Acta Materialia 169 (2019) 172–183

Contents lists available at ScienceDirect

Acta Materialia

journal homepage: www.elsevier.com/locate/actamat

Full length article

Doping α-Al_2O_3 to reduce its hydrogen permeability: Thermodynamic assessment of hydrogen defects and solubility from first principles

Vrindaa Somjit [a, b], Bilge Yildiz [a, b, c, *]

[a] Laboratory for Electrochemical Interfaces, Massachusetts Institute of Technology, 77 Massachusetts Avenue, Cambridge, MA, 02139, USA
[b] Department of Materials Science and Engineering, Massachusetts Institute of Technology, 77 Massachusetts Avenue, Cambridge, MA, 02139, USA
[c] Department of Nuclear Science and Engineering, Massachusetts Institute of Technology, 77 Massachusetts Avenue, Cambridge, MA, 02139, USA

ARTICLE INFO

Article history:
Received 15 September 2018
Received in revised form
22 December 2018
Accepted 19 February 2019
Available online 21 February 2019

Keywords:
Alumina (α-Al_2O_3)
Density functional theory (DFT)
Point defects
Hydrogen embrittlement
Hydrogen permeation barrier

ABSTRACT

This paper assesses the role of doping on the hydrogen permeability and electronic properties of α-Al_2O_3. Formation energies of intrinsic and extrinsic defects in α-Al_2O_3 were calculated using density functional theory. Using these energies as input, a thermodynamic model was utilized to identify the equilibrium defect concentrations (barring hydrogen defects) in undoped and doped α-Al_2O_3 under aluminization conditions of 1100 K, over a range of p_{O2} at a fixed doping level of 1 ppm. Defect concentrations calculated at 1100 K under p_{O2}-rich conditions were used as input to establish hydrogen and electronic defect concentrations under functional conditions of 300 K, over a range of p_{H2}. The effect of dopants on the fraction of free hydrogen interstitials, which has implications on diffusivity, and the overall hydrogen solubility, was found to be substantial and distinct. Relative to the undoped case, Mg-doping increased the concentration of free hydrogen interstitials, the primary diffusing species, by 10^7 times, whereas Ti-, Si-, Fe-, Cr-doping eliminated it to negligible amounts. Comparing the impact on total hydrogen solubility, Mg-doping increased it by 10^4 times; Fe- and Cr-doping increased it negligibly by ~1.5 times. In contrast, Ti- and Si- doping decreased it to nearly 1/3 that of the undoped case. Analyzing the role of isolated defect concentrations and binding energies of defect complexes helps elucidate these effects. Effect of dopant concentrations of 10 and 100 ppm was also investigated, with the conclusion that doping with Si and Ti at 1 ppm is the best strategy to reduce hydrogen diffusivity and solubility by the greatest amount. The findings aid in the design of effective hydrogen permeation barrier layers for use in hydrogen storage and transport infrastructure as well as in the understanding of defect states in Al_2O_3 used in electronic devices, such as resistive switching.

1. Introduction

The past few years have witnessed a growing interest in the study of hydrogen in oxides. One area of key focus has been on understanding the factors influencing hydrogen permeability in barrier oxides like Al_2O_3 [1–5]. Hydrogen permeation barriers (HPBs) are needed for high temperature applications such as that in nuclear reactors to prevent tritium escape into the environment [6], as well as for room temperature applications such as preventing embrittlement of steels used in hydrogen storage and transport infrastructure [7]. This will play a key role in enabling the hydrogen economy.

From the various material classes considered for use as HPBs on steels [8], it appears that α-Al_2O_3 performs as one of the best [6,9]. Its experimentally determined permeation reduction factor is the highest among candidate HPB materials [6]. The activation energy for hydrogen diffusion in the steel lattice is only 0.08 eV [10], whereas for diffusion in sintered alumina it is 1.89 eV [11]. This results in hydrogen diffusivity of alumina being more than 10^{20} times lower than that of steel. Moreover, the low solubility of hydrogen in α-Al_2O_3 [9], its good adherence [12], and its high chemical stability under reducing conditions [13], make it an ideal choice for use as a HPB.

Computational studies have helped better understand the behavior of hydrogen in α-Al_2O_3. Belonoshko et al. [14] computed the diffusivity of neutral H in bulk α-Al_2O_3 to be ~10^{-29} m^2/s at

* Corresponding author. Department of Nuclear Science and Engineering & Department of Materials Science and Engineering, Massachusetts Institute of Technology, 77 Massachusetts Avenue, Building 24-210, Cambridge, MA, 02139, USA.
E-mail address: byildiz@mit.edu (B. Yildiz).

https://doi.org/10.1016/j.actamat.2019.02.031
1359-6454/

room temperature. Zhang et al. [4] studied the interactions of native defects of α-Al_2O_3 with hydrogen and identified that hydrogen predominantly exists as a proton attached to a lattice oxygen, a proton trapped at the aluminum vacancy site, and as a proton trapped at the oxygen vacancy site. Infrared absorption measurements of H-defects in α-Al_2O_3 [15,16] support this as well, revealing that in single crystal α-Al_2O_3, hydrogen is present as an interstitial defect, forming an OH^- ion. These OH^- defects are frequently associated with other point defects in charge-compensating roles, such as triply-charged aluminum vacancies [16]. The study on H_2 incorporation on the clean (0001) α-Al_2O_3 surface proposed that the reason behind the superior performance of α-Al_2O_3 as a hydrogen permeation resistant coating is the endothermicity and high energy barrier for surface to sub-surface incorporation of hydrogen [5]. The role of crystal orientation on hydrogen diffusion into α-Al_2O_3 has also been studied, with the conclusion that the $\left(1\bar{1}20\right)$ surface is more susceptible to hydrogen incorporation than (0001) [3].

While the above studies help characterize the behavior of hydrogen in α-Al_2O_3, insofar, to *improve* the performance of α-Al_2O_3 as a HPB, research has primarily been devoted to identifying deposition processes to improve its adherence to the underlying steel [17–19]. However, it is well established that point defects and impurities affect the electrical and transport properties of materials, especially that of α-Al_2O_3 [20].

Thus, the goal of this work is to quantitatively resolve and engineer the effect of point defects, i.e., dopants on the solubility and diffusivity of hydrogen defects in α-Al_2O_3. A similar framework to that established by Youssef et al. [21] for reducing the H-solubility in and increasing the H-evolution kinetics on ZrO_2, another barrier oxide, has been adopted and advanced in this paper to further enhance the properties of α-Al_2O_3 as a permeation barrier.

We note here that the results of this study and the framework utilized are also relevant for other applications that involve use of dopants and hydrogen to change electronic properties of oxides. One such area is resistive switching, where much is left to be resolved regarding the role of counter charges and reactions in device performance. Multiple studies have emphasized the role of dopants in oxide electrolytes to improve the performance of ECM cells by affecting mobility, eliminating the need for forming, etc. [22,23]. It is also important to understand the defect states of hydrogen in oxides, for such devices show sensitivity to environmental conditions such as humidity, as highlighted by Tappertzofen et al. [24]. Given that these studies have been largely empirical, quantitative studies such as this paper can help unequivocally establish the predominant compensation mechanisms in such hydrogenated systems as well as those based on protonation and deprotonation of oxides to enable switching, such as VO_2 [25] and indium-zinc-oxide [26].

In this work, the formation energies of defects in α-Al_2O_3 were calculated and used to identify the predominant defects in undoped and doped α-Al_2O_3 (without hydrogen) under 1100 K, aluminization conditions, over a range of p_{O2}. Ionic defects cannot re-equilibrate under low temperature, functional conditions of 300 K. These defect concentrations as established at high p_{O2} were thus kept fixed, and hydrogen and electronic defect concentrations were then found under operating conditions at room temperature, over a range of p_{H2}. Different dopants appear to have different effects on the total hydrogen solubility in this material, and also on the relative fractions of free hydrogen interstitials versus bound hydrogen complexes. The dopants also significantly alter the electrical properties of α-Al_2O_3. Note that throughout this paper, defects are denoted using the Kröger-Vink notation.

2. Methodology

2.1. DFT calculations

The energetics of the $2 \times 2 \times 1$ perfect supercell (a = 9.62 Å, c = 13.13 Å) and of all the defects were calculated using density functional theory (DFT) using a plane-wave basis set, projector-augmented wave pseudopotentials [27] and the Perdew-Burke-Ernzerhof (PBE) parameterization of the generalized gradient approximation (GGA) [28] as the exchange-correlation functional, as implemented in the Vienna ab initio Simulation Package (VASP) [29] v.5.4.1. A kinetic energy cutoff of 520 eV and a gamma-centered $2 \times 2 \times 2$ k-point mesh were used, resulting in a convergence accuracy of <1 meV/atom. All calculations were performed with a Gaussian smearing width of 0.05 eV and spin-polarized setting. Atomic positions were relaxed until the force on each atom was below 0.05 eV/Å. The first order Makov-Payne (MP1) correction [30] was adopted to account for the finite-size errors arising from periodic boundary conditions as imposed by DFT. We used the dielectric constant of α-Al_2O_3 as 9 [31]. Comparison of the results of these settings with experiments and prior GGA calculations, and relaxed structures of the native defects (vacancies and interstitials of Al and O) can be found in Table S1 and Fig. S1 respectively of the Supplementary Information (SI). Details of the hydrogen defects studied (interstitials, complexes with Al-vacancies, O-vacancies and dopants) are elaborated upon in Section 3.3. The substitutional dopants considered were Mg, Si, Ti, Fe and Cr. These are common acceptor and donor substitutional impurities in α-Al_2O_3 [20]. Systematically studying this range of dopants helps compare and contrast the effect on electrical properties and hydrogen solubility of α-Al_2O_3 doped with a prototypical acceptor $\left(Mg'_{Al}\right)$, a prototypical donor $(Si^{\cdot}_{Al})$, and dopants that show multiple charge states (Ti^q_{Al}, Fe^q_{Al}, Cr^q_{Al}), thus covering a broad spectrum of possibilities.

2.2. Thermodynamic model to evaluate defect concentrations in native and doped α-Al_2O_3 at 1100 K in oxygen atmosphere

The concentration N_i (in units of per f.u. of α-Al_2O_3) of defect i is given by the equation [32].

$$N_i = \frac{N^i_{sites} N^i_{conf}}{N^i_{conf} + exp\left(\frac{E^i_f}{kT}\right)} \approx N^i_{sites} N^i_{conf} exp\left(\frac{-E^i_f}{kT}\right) \quad (1)$$

where $E^i_f = E^{def}_{tot} - E^{perf}_{tot} - \sum_j \Delta n_j \mu_j + q_i \mu_e$, the formation energy of defect i with charge q_i. The notations are as follows: N^i_{sites} = total number of sites over which N_i defects of type i can be distributed; N^i_{conf} = number of equivalent configurations in which the defect i can be incorporated on a single site; E^{def}_{tot} and E^{perf}_{tot} = DFT total energies of the defect and perfect supercells; Δn_j = the difference in the number of $j(Al,\ O)$ atoms in the defect and perfect supercell; μ_j chemical potential of $j(Al,\ O)$ in the system; μ_e = electrochemical potential for charge, defined as $\mu_e = E_{VBM} + \mu_f$, where E_{VBM} is the valence band maximum of the perfect supercell and μ_f is the Fermi level relative to the valence band maximum; k = Boltzmann constant; T = temperature.

The chemical potential of oxygen μ_O is given as

$$\mu_O(T,P_{O_2}) = \frac{1}{2}\left[E_{O_2}^{DFT} + E_{over} + \mu_{O_2}^0\left(T,P^0\right) + kTln\left(\frac{P_{O_2}}{P^0}\right)\right] \quad (2)$$

where $E_{O_2}^{DFT}$ = DFT energy of the O_2 molecule; E_{over} = correction for the O_2 overbinding error caused by GGA, taken as 1.36 eV as identified by Wang et al. [33]; $\mu_{O_2}^0(T,P^o)$ is the difference in chemical potential of O_2 gas between $T = 0K$ and the temperature of interest, at a reference pressure of $P^o = 1\ atm$, as obtained from thermochemical tables [34]; P_{O_2} is the partial pressure of oxygen gas.

The chemical potential of Al can be directly obtained from μ_O, and is given as

$$\mu_{Al}(T,P_{O_2}) = \frac{1}{2}\left[E_{Al_2O_3}^{DFT} - 3\mu_O(T,P_{O_2})\right] \quad (3)$$

where $E_{Al_2O_3}^{DFT}$ is the DFT energy of one formula unit of the perfect crystal of α-Al_2O_3.

Equation (1) does not include the chemical potential of the dopant, μ_M , as we *fix* the total concentration of each dopant considered at 1 ppm. Thus, the system is no longer thermodynamically open to the dopant M , therefore μ_M does not appear in the equation. This reflects the experimental conditions of addition of dopants in fixed concentrations during the formation of Al_2O_3 film. 1 ppm is simply a representative doping concentration, chosen to be within the solubility limit of the various dopants in α-Al_2O_3 and to ensure that the dilute defect approximation is still valid.

The derivation of Equation (1) and approximations used can be found in SI Section S3. The comparison of our DFT calculations of O_2 and H_2 molecules with experiments and previous theoretical work can be found in SI Table S2.

2.3. Thermodynamic model to evaluate defect concentrations in native and doped α-Al_2O_3 at 300 K in hydrogen atmosphere

The concentrations of various hydrogen defects considered at 300 K is given by

$$N_{H_i^q} \approx N_{sites}^{H_i^q} N_{conf}^{H_i^q} exp\left(\frac{-E_f^{H_i^q}}{kT}\right) \quad (4)$$

$$N_{[X-nH]^q} = \frac{N_{conf}^{[X-nH]^q}}{N_{conf}^{X^{q_1}}\left(N_{sites}^{H_i^{q_2}} N_{conf}^{H_i^{q_2}}\right)^n} N_{X^{q_1}}\left(N_{H_i^{q_2}}\right)^n exp\left(\frac{E_b}{kT}\right) \quad (5)$$

where H_i^q signifies hydrogen interstitials and $[X-nH]^q$ signifies hydrogen complexes considered, with $X = V_{Al}$ or V_O or M_{Al} (aluminum vacancy, oxygen vacancy, substitutional dopant on Al site, respectively) and n = number of hydrogen interstitials forming the complex. q is the charge state of the defect. E_b is the binding energy of the complex, given as $E_b(AB) = E_f^A + E_f^B - E_f^{AB}$. Only those complexes with positive binding energy and which form realizable charges (q_1, q_2) upon dissociation are considered (see SI Table S3 for list).

These equations result from minimization of the constrained grand canonical potential (derivation in SI Section S5), in which we consider the system to be open to hydrogen and electrons, and closed to aluminum and oxygen. The experimentally determined activation energies for O, Al, and H diffusion in polycrystalline α-Al_2O_3 are ~6 eV [35], ~4 eV [35], and ~1.89 eV [11] respectively. This wide difference in activation energies results in H being comparatively more mobile than Al and O. Thus, H can diffuse through the system and equilibrate with the environment even at low temperatures of 300 K, whereas Al and O (and other ionic defects in general), due to their larger sizes, are immobile at such low temperatures and do not equilibrate with the environment. Native and dopant defect concentrations are thus *fixed* to the values obtained for each charge state at 1100 K, O-rich conditions.

The chemical potential of hydrogen is computed as

$$\mu_H(T,\ P_{H_2}) = \frac{1}{2}\left[E_{H_2}^{DFT} + \mu_{H_2}^o(T,P^o) + k_BTln\left(\frac{P_{H_2}}{P^o}\right)\right], \quad (6)$$

where $E_{H_2}^{DFT}$ = DFT energy of a H_2 molecule; $\mu_{H_2}^o(T,P^o)$ is calculated from thermochemical tables, analogous to $\mu_{O_2}^o(T,P^o)$; P_{H_2} is the partial pressure of hydrogen gas.

The above equations are solved with the constraint $N_{X^{q_1}}^{tot} = N_{X^{q_1}} + \sum_{n,q} N_{[X-nH]^q}$, ($X = V_{Al}$ or V_O or M_{Al}). The concentration of hydrogen interstitials, defect complexes and the remaining free isolated native and dopant defects can thus be calculated.

2.4. Kröger-Vink formalism to calculate defect equilibria

The main tenet of a defect equilibria plot (also called a Kröger-Vink diagram) is that at a given temperature and p_{O2} (or p_{H2}), charge-neutrality needs to be satisfied:

$$\sum_i q_i N_i + p_v - n_c = 0 \quad (7)$$

here, N_i = concentration of point defect i of charge q_i, p_v = concentration of holes in the valence band and n_c = concentration of electrons in the conduction band, which are calculated by integrating the electronic density of states $g(E)$

$$p_v = \int_{-\infty}^{E_{VBM}} g_v(E)\frac{dE}{1+exp\left(\frac{\mu_e - E}{kT}\right)} \quad (8a)$$

$$n_c = \int_{E_{CBM}}^{\infty} g_c(E)\frac{dE}{1+exp\left(\frac{E-\mu_e}{kT}\right)} \quad (8b)$$

E_{CBM} is the energy of the conduction band minimum.

Each of the terms in Equation (7) is a function of the Fermi level μ_f. Solving for this μ_f that achieves charge neutrality at each p_{O2} and p_{H2} using a standard root-finding algorithm, we can then obtain the concentration N_i of point defect i and the concentration of valence band holes p_v and conduction band electrons n_c at a particular temperature over a range of p_{O2} and p_{H2}.

3. Results and discussion

3.1. Defect equilibria in undoped α-Al_2O_3 at 1100 K in oxygen atmosphere

Fig. 1 presents the calculated defect equilibria of undoped α-Al_2O_3 at 1100 K. The formation energies used as input to generate such Kröger-Vink diagrams and their implications are discussed in SI Fig. S2.

GGA-PBE [28] is known to underestimate the band gap of semiconductors and insulators, as it does for α-Al_2O_3 as well (SI Table S1). In many cases, it also fails to predict charge localization originating from narrow bands (as in transition metal oxides) or due to local lattice distortions around defects. This can affect the computed formation energies and defect transition levels, which can affect the trends in calculated defect concentrations. Therefore,

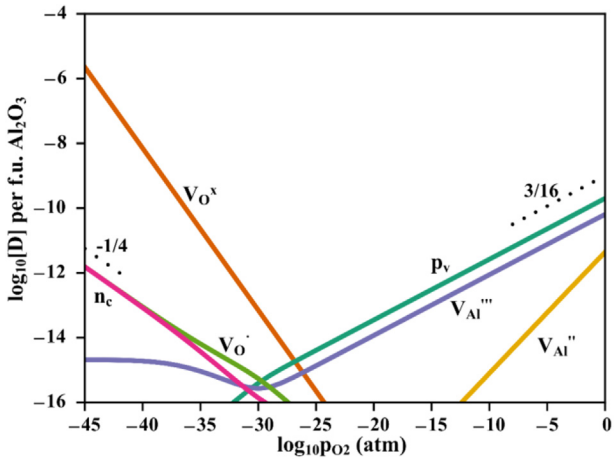

Fig. 1. Kröger-Vink diagram of undoped α-Al_2O_3 at 1100 K. Only defects with concentration [D] > 10^{-16} per f.u. are shown. Point defects are represented using Kröger-Vink notation, n_c denotes conduction band electrons and p_v denotes valence band holes.

it is important to compare the GGA-PBE computed formation energies and defect levels with more accurate (but more computationally expensive) functionals like the Heyd-Scuseria-Ernzerhof (HSE) [36] hybrid functional. Comparison with calculations by Choi et al. [37], who used HSE, show that GGA-PBE here successfully captures the trends in formation energies and defect levels in α-Al_2O_3. This fortuitous correspondence is likely because α-Al_2O_3 does not exhibit any charge localization arising from narrow bands or lattice distortions. Thus, from a semi-quantitative standpoint, the trends in predicted defect concentrations will remain the same, with no significant impact on the results of this study. This comparison and discussion is further elaborated upon in SI Section S8.

At high p_{O2}, p-type conductivity is exhibited, where holes p_v are compensated by V_{Al}'''. At strongly reducing atmospheres, V_O^x is the predominant defect, and n-type conductivity is exhibited, where electrons n_c are compensated by $V_O^{\cdot}$. In the high (low) p_{O2} cases, compensation of V_{Al}''' ($V_O^{\cdot}$) does not occur via ionic defects like $V_O^{\cdot\cdot}$ (V_{Al}''') to form a Schottky quintet or $Al_i^{\cdot\cdot\cdot}$ (O_i'') to form a Frenkel pair, as such defects have prohibitively high formation energies (>4 eV, see SI Table S5). Compensation by partially charged $V_O^{\cdot}$, $Al_i^{\cdot\cdot}$, $Al_i^{\cdot}$ (V_{Al}'', V_{Al}', O_i') would similarly require high formation energies. The equilibrium Fermi level established in both the cases is such that compensation by electronic defects is energetically more favorable. Therefore, in order to enhance the electrical conductivity of undoped α-Al_2O_3, one could either process the sample under p_{O2}-rich conditions to increase the concentration of V_{Al}''' and holes, or alternatively, process the sample under p_{O2}-poor conditions to increase the concentration of $V_O^{\cdot}$ and electrons.

Our calculated plot captures the experimental defect compensation mechanism at high p_{O2} successfully, with the computed slope of ~0.19 in good accordance with the experimental p_{O2} dependence [38]. At intermediate p_{O2}, p_{O2}-independent extrinsic ionic conductivity has been observed experimentally [38], given the high levels of impurities found in nominally 'pure' single crystal α-Al_2O_3 (for instance, Si reaches up to ~100 ppm in the study by Kitazawa [38]), and the high energies of formation of intrinsic Schottky/Frenkel defects mentioned in the previous paragraph. We therefore see no such flat region in our calculated plot, as our calculations consider only pure α-Al_2O_3. At low p_{O2}, although our computed plot captures the experimentally observed n-type conductivity [38], the computed slope is 0.25, in contrast to the range experimentally observed ~0.15–0.2 [38]. We attribute the difference to the presence of V_O^x and $V_O^{\cdot}$ defects (known as F and F+ color centers respectively). The samples used in experiments were either heated to very high temperatures (>1700 °C) to obtain steady state conductivity measurements or were hot-pressed [38]. This heating and holding at high temperature (for example, for 5 h at 1800 °C [39]) is done to remove the F and F+ color centers in α-Al_2O_3, as exemplified by Levy [39]. Thus, in the experiments conducted, the defect species at low p_{O2} are most likely electrons compensated by $V_O^{\cdot\cdot}$. In our computed Kroger-Vink diagram, at low p_{O2}, we see that the predominant charged defect species are $V_O^{\cdot}$ compensated by electrons. We see V_O^x to be the predominant defect overall. These electron-vacancy associated defects and cannot be 'annealed' out and dissociated at the temperature (1100K) in these calculations.

Another difference between the experimental conductivity plots and our calculated Kroger-Vink diagram is the p_{O2} at which transition between p-type to n-type conductivity occurs. The calculated transition p_{O2} is ~10^{-32} atm, as compared to 10^{-12} atm in experiments at 1500 K [38]. This difference can be attributed to the higher temperatures implemented in conductivity experiments and to the impurities present in the experimental samples, which alter the transition p_{O2}. These effects can be seen in SI Fig. S4.

Despite these differences, the corroboration of the computed slopes and defect compensation mechanisms with experimental studies at high p_{O2} and the logical justification for the discrepancy at low p_{O2}, are encouraging and ratify the robustness of our model. Moreover, since we are concerned with mainly the high p_{O2} results for establishing hydrogen defect concentrations, the validation of our computed trends with that of experiments in this regime gives us confidence in the results presented in the following sections.

3.2. Defect equilibria in doped α-Al_2O_3 at 1100 K in oxygen atmosphere

Fig. 2 shows the defect equilibria established in α-Al_2O_3 doped with Mg, Si, Ti, Fe and Cr at 1100 K. The total dopant concentrations are fixed at 1 ppm.

Fig. 2a shows the defect equilibria established in Mg-doped α-Al_2O_3. Mg exhibits predominantly a 2 + charge state on the Al^{3+} site (Mg_{Al}') and thus is an acceptor dopant. At high p_{O2}, Mg_{Al}' is compensated by holes. The hole concentration is entirely dictated by the concentration of Mg_{Al}' and is nearly 10^4 times higher than in the undoped case. Thus, the electronic conductivity of α-Al_2O_3 can be increased at high p_{O2} by doping with Mg. In contrast, the concentration of V_{Al}''' is lowered by nearly 10^{11} times. An increase in other positively charged defects, namely $V_O^{\cdot\cdot}$ and $Al_i^{\cdot\cdot\cdot}$ is observed at high p_{O2}, which was not seen in the undoped case. As the p_{O2} is reduced, compensation of Mg_{Al}' is predominantly first by $V_O^{\cdot\cdot}$ and $Al_i^{\cdot\cdot\cdot}$ and then at extreme reducing regimes, compensation is by $V_O^{\cdot}$. V_O^x also exhibits significant concentrations as p_{O2} is reduced. The concentration of holes is found to decrease with decrease in p_{O2}. Conductivity experiments on 10 ppm Mg-doped single crystal α-Al_2O_3 [40] revealed that the electronic conductivity decreased monotonically, while the ionic conductivity increased and approached a constant value with decrease in p_{O2}. The electronic conductivity was attributed to holes, but the study was unable to determine whether to attribute ionic conductivity to $V_O^{\cdot\cdot}$ or $Al_i^{\cdot\cdot\cdot}$. The same trend is seen in our calculated Kröger-Vink plot, with the concentration of holes decreasing and the concentration of $V_O^{\cdot\cdot}$ and $Al_i^{\cdot\cdot\cdot}$ increasing and approaching a (near-equal) constant value with decreasing p_{O2}. Unlike our calculated plot, a slight increase in ionic conductivity due to $V_O^{\cdot}$ is not observed experimentally, possibly due to use of hot-pressed samples/high experimental temperatures which anneal out such electron-vacancy associated defects, as explained in Section 3.1.

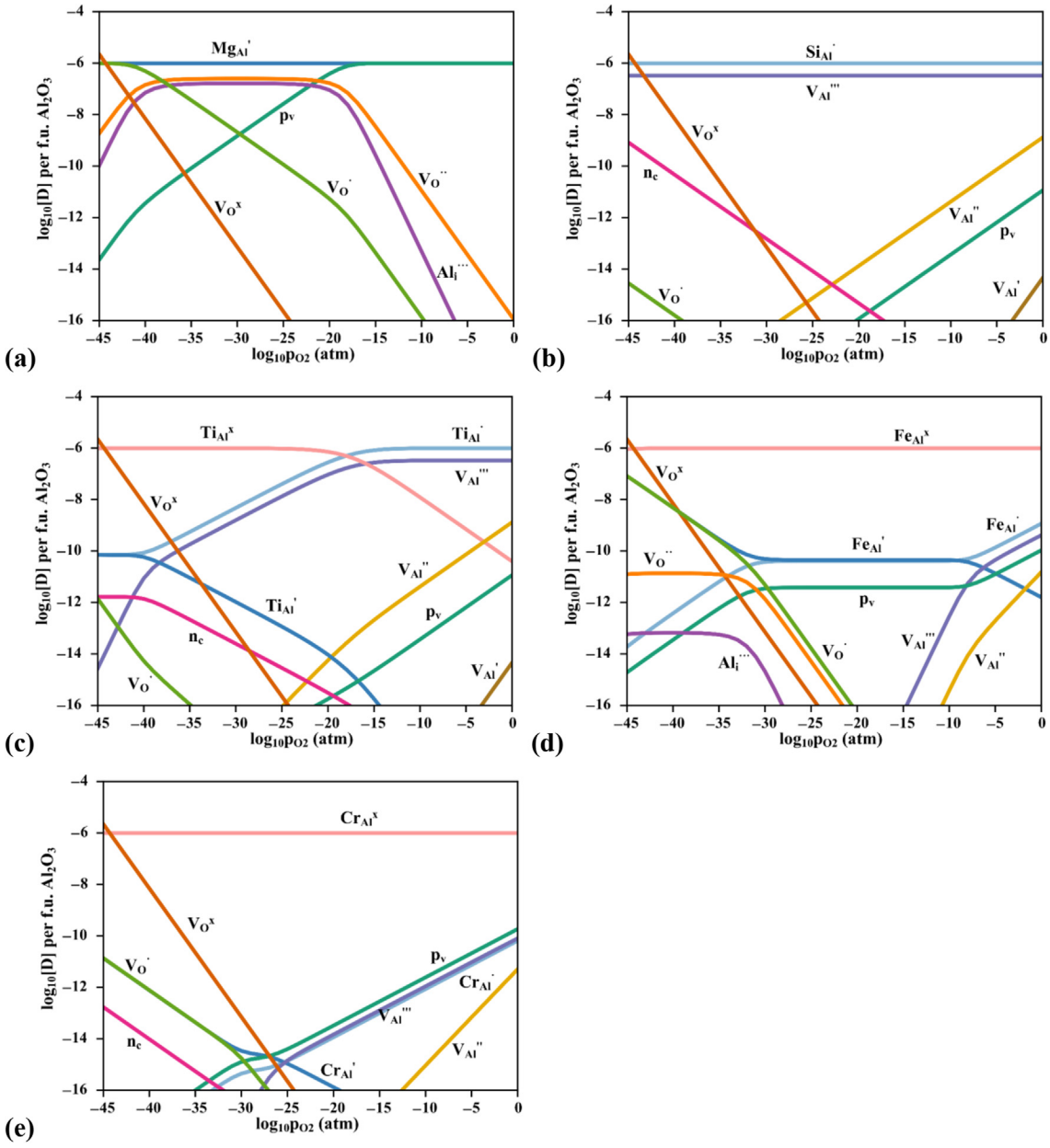

Fig. 2. Defect equilibria in (a) Mg-doped (b) Si-doped (c) Ti-doped (d) Fe-doped (e) Cr-doped α-Al_2O_3 at 1100 K with dopant concentration fixed at 1 ppm. Only defects with concentration [D]>10^{-16} per f.u. are shown. Point defects are represented by Kröger-Vink notation, n_c denotes conduction band electrons and p_v denotes valence band holes.

At the other extreme, Fig. 2b shows the defect equilibria established in Si-doped α-Al_2O_3. Si exhibits predominantly a 4+ charge state on the Al^{3+} site ($Si_{Al}^{\cdot}$) and thus acts as a donor. Unlike $Mg_{Al}^{'}$, which is compensated by an electronic defect, $Si_{Al}^{\cdot}$ is compensated almost entirely by the ionic defect $V_{Al}^{'''}$ (and not electrons) across the p_{O2} range studied. The Fermi level established in Si-doped α-Al_2O_3 across the p_{O2} range is too far from the computed conduction band minimum to result in compensation by electrons (see SI Fig. S5 for calculated equilibrium Fermi levels at high and low p_{O2} for all doped cases). Thus, the concentration of $V_{Al}^{'''}$ can be entirely tuned by controlling the donor dopant concentration, and thus, it is increased by over 10^3 times upon 1 ppm Si doping. Thus, the ionic conductivity of α-Al_2O_3 can be increased by addition of a donor dopant like Si. The concentration of holes is 10 times lower than the undoped case at high p_{O2}. Density measurements on Si-doped single-crystal α-Al_2O_3 also suggest compensation of Si^{4+} by $V_{Al}^{'''}$ [41].

In Ti-doped α-Al_2O_3, we see that at high p_{O2}, Ti^{4+} ($Ti_{Al}^{\cdot}$) is the predominant charge state and it is compensated by $V_{Al}^{'''}$. Similar to the Si-doped case, an increase in the concentration of $V_{Al}^{'''}$ as compared to the undoped case is seen, by over 10^3 times. Concentration of holes is 10 times lower than the undoped case at high p_{O2}. Thus, ionic conductivity of α-Al_2O_3 can be increased by addition of Ti under high p_{O2} conditions. As p_{O2} is reduced, Ti^{3+} becomes the predominant charge state (Ti_{Al}^{x}), and the concentrations of V_{Al}^{q} defects reduce as well, decreasing ionic conductivity. A steady increase in the concentration of $Ti_{Al}^{'}$ and electrons is seen as well, along with V_O^x and $V_O^{\cdot}$. Experimental studies on Ti-doped single crystal α-Al_2O_3 [41,42] have also observed that $V_{Al}^{'''}$ primarily compensates for $Ti_{Al}^{\cdot}$ at high p_{O2}. Optical absorption measurements [42] with varying p_{O2} revealed that at high p_{O2}, $Ti_{Al}^{\cdot}$ is the predominant charge state, and as p_{O2} decreases, concentration of

$Ti_{Al}^{\cdot}$ decreases while that of Ti_{Al}^{x} increases. Electrical conductivity studies in the same paper revealed that as p_{O2} decreases, ionic conductivity (attributed to $V_{Al}^{'''}$) decreases, electronic conductivity increases (attributed to electrons). The same trend is captured by our calculations.

In Fe-doped α-Al_2O_3, as seen in Fig. 2d, Fe^{3+} $\left(Fe_{Al}^{x}\right)$ is the predominant charge state across the p_{O2} range studied. At high p_{O2}, the concentration of $Fe_{Al}^{\cdot}$ is only ~10^{-9} per f.u., 10^3 times lower than the total concentration of Fe in the lattice (1 ppm). The concentration of the compensating $V_{Al}^{'''}$ to 4×10^{-10} f.u., only 10 times higher than that in the undoped case. Experimental studies on Fe-doped single crystal [43] and polycrystalline [44] α-Al_2O_3 have also concluded that Fe_{Al}^{x} is the predominant defect in Fe-doped α-Al_2O_3. The model based on conductivity tests [43] claimed that high p_{O2} conductivity is due to holes, with a slope of +3/16. While we see holes having a significant concentration in our calculated plots, with a p_{O2} dependency of +3/16, holes are not the predominant charged defect in our case. $Fe_{Al}^{\cdot}$ is the predominant charged defect, compensated by $V_{Al}^{'''}$, with the same p_{O2} dependency as that of holes and the experiments. The conductivity studies [43] did not consider calculating the ionic transference number by measuring EMF as a function of p_{O2}, and analysis was done assuming $Fe_{Al}^{'}$ and Fe_{Al}^{x} as the only charge states that Fe expresses, so it is possible that the presence of ionic conductivity due to $V_{Al}^{'''}$ was missed. At low p_{O2}, our model reveals that the main defect compensation mechanism is $V_O^{\cdot\cdot}$ compensating $Fe_{Al}^{'}$. However, creep tests on polycrystalline α-Al_2O_3 concluded that $Al_i^{\cdot\cdot\cdot}$ is the predominant defect [44]. Although the creep rates gave good agreement with p_{O2} dependency of both $V_O^{\cdot\cdot}$ and $Al_i^{\cdot\cdot\cdot}$, the better match of the diffusion coefficient of $Al_i^{\cdot\cdot\cdot}$ with that calculated in creep tests resulted in the conclusion that $Al_i^{\cdot\cdot\cdot}$ is the main defect. The fact that we are considering single crystal α-Al_2O_3 in this study, and given that α-Al_2O_3 grain boundaries are fast diffusion pathways for oxygen (which precluded its consideration as a rate limiting step in creep) could be the reason behind the difference at low p_{O2}.

In Cr-doped α-Al_2O_3, as seen in Fig. 2e, similar to the case of Fe-doped α-Al_2O_3, Cr^{3+} $\left(Cr_{Al}^{x}\right)$ is the predominant charge state across the p_{O2} range. At high p_{O2}, the concentration of $Cr_{Al}^{\cdot}$ is only ~10^{-11} per f.u. $Cr_{Al}^{\cdot}$ is compensated by $V_{Al}^{'''}$; the concentration of which is 8×10^{-11} per f.u., nearly equal to that in the undoped case. Apart from $Cr_{Al}^{\cdot}$ and $V_{Al}^{'''}$, holes are also seen to have predominant concentration at high p_{O2}. Except for Cr_{Al}^{x}, $Cr_{Al}^{\cdot}$ and $Cr_{Al}^{'}$, no other charge states of Cr (+5, +6) are found to have significant concentrations in the p_{O2} range considered. To our knowledge, no experimental conductivity studies have been conducted for Cr-doped α-Al_2O_3, but Cr is known to be primarily an isovalent dopant in α-Al_2O_3 [41]. This is reflected in our plots.

Thus, from the above analysis, at high p_{O2}, α-Al_2O_3 formation conditions, to increase the electronic conductivity of α-Al_2O_3, acceptor doping such as that with Mg should be employed; to increase the cationic conductivity of α-Al_2O_3, donor doping such as that with Si or Ti, which exhibit predominantly 4 + charge states, should be employed. Fe and Cr doping will prove to be unsatisfactory dopants if the aim is to increase electronic/ionic conductivity, as these dopants are primarily isovalent in the α-Al_2O_3 lattice. The trends observed above can further be rationalized from the equilibrium Fermi levels established, which is elaborated upon in SI Fig. S5.

3.3. Hydrogen defects in α-Al_2O_3

Before going into the defect equilibria of hydrogen and electronic defects at 300 K, H_2 gas environment conditions, we first define the relevant hydrogen defects in α-Al_2O_3. The defects considered were: mono-hydrogen interstitials H_i^q, Al vacancy-H complexes $[V_{Al} - nH]^q$, substitution in the O site H_O^q (denoted as $[V_O - H]^q$ in Section 2.3) and dopant-H complexes $[M_{Al} - H]^q$. We do not consider H complexes with native interstitials as the latter have high energies of formation across most of the Fermi level range (see SI Fig. S2), rendering their concentrations and thereby their complexes with hydrogen, negligible. Fig. 3 shows the fully relaxed atomic configurations of some of the key hydrogen defects. In $H_i^{\cdot}$, hydrogen is oriented towards the empty octahedral interstitial site, as a proton attached to one of the 6 degenerate oxygen atoms. This orientation matches previous experimental [15,16] and theoretical [4] studies. Given that Al vacancies are known to be 'hydrogen sinks' in Al_2O_3 [45], it is important to consider Al vacancy-H clusters. In all $[V_{Al} - nH]^q$ clusters, hydrogen atoms exist as protons attached to oxygen atoms, pointing towards the cation vacancy center.

The tendency to add/remove a hydrogen atom to an existing $[V_{Al} - nH]^q$ complex is determined by a positive/negative binding energy:

$$E_b\left([V_{Al} - nH]^q\right) = E_f^{[V_{Al}-(n-1)H]^{q-1}} + E_f^{H_i^{\cdot}} - E_f^{[V_{Al}-nH]^q} \quad (9)$$

From Table 1, it is clear that $[V_{Al} - nH]^q$ upto $n = 5$ are stable.

While other charge states of these defect complexes are theoretically possible, the number of possibilities are intractable when $n > 1$. Intuitively, we believe that the charge states listed in Table 1 will be the predominant charge states, given that the $V_{Al}^{'''}$ is known to be a very attractive site for protons, as observed from experimental infrared absorption peaks in cooled γ-irradiated single crystal α-Al_2O_3 specimen [47] and from theoretical studies [45]. In $H_O^{\cdot}$ the hydrogen occupies the oxygen vacancy site. Charge density plots and local density of states (shown in SI Fig. S6) reveal that hydrogen multicenter bonds are formed between the reactive hydrogen and the nearest neighbor Al cations. This also explains the high binding energy of the complex (3.12 eV, see SI Table S3).

3.4. Defect concentration profiles at 300 K in hydrogen atmosphere

We examine next the concentrations of hydrogen and electronic defects established at 300 K over a range of p_{H2}, while keeping the individual ionic defect concentrations fixed as found in undoped and doped α-Al_2O_3 at 1100 K high p_{O2} conditions. At such low temperatures, binding energy effects become significant. As a result, while the *total* native and dopant concentrations are fixed, hydrogen may bind to these defects, thus the concentration of isolated native and dopant defects may decrease and the concentration of defect complexes increase.

Fig. 4a shows the defects in undoped α-Al_2O_3. We see that the predominant defect is $[V_{Al} - 3H]^x$. If one compares this with Fig. 1, it is readily noticed that the concentration of $[V_{Al} - 3H]^x + [V_{Al} - 4H]^{\cdot}$, whose constituent defects are $V_{Al}^{'''}$ and $H_i^{\cdot}$, is nearly equal to that of $V_{Al}^{'''}$ established at 1100 K, $p_{O2} = 1$ atm (6.3×10^{-11} per f.u.). The concentration of free hydrogen interstitials $H_i^{\cdot}$ is ~10^{-16} per f.u. The concentrations of $[V_{Al} - H]^{''}$, $[V_{Al} - 2H]^{'}$ and $[V_{Al} - 5H]^{\cdot\cdot}$ are not significant, as all the $[V_{Al} - nH]^q$ complexes compete for the fixed number of $V_{Al}^{'''}$ sites. The significantly high binding energies of the clusters up to n = 4 as seen in Section 3.3 results in the predominance of $[V_{Al} - 3H]^x$ and $[V_{Al} - 4H]^{\cdot}$. Moreover, concentration of $[V_{Al} - 5H]^{\cdot\cdot}$ is lower due to the comparatively lower binding energy and due to the $(N_{H_i^q})^n$ term involved in determining its concentration, which rapidly reduces the right-

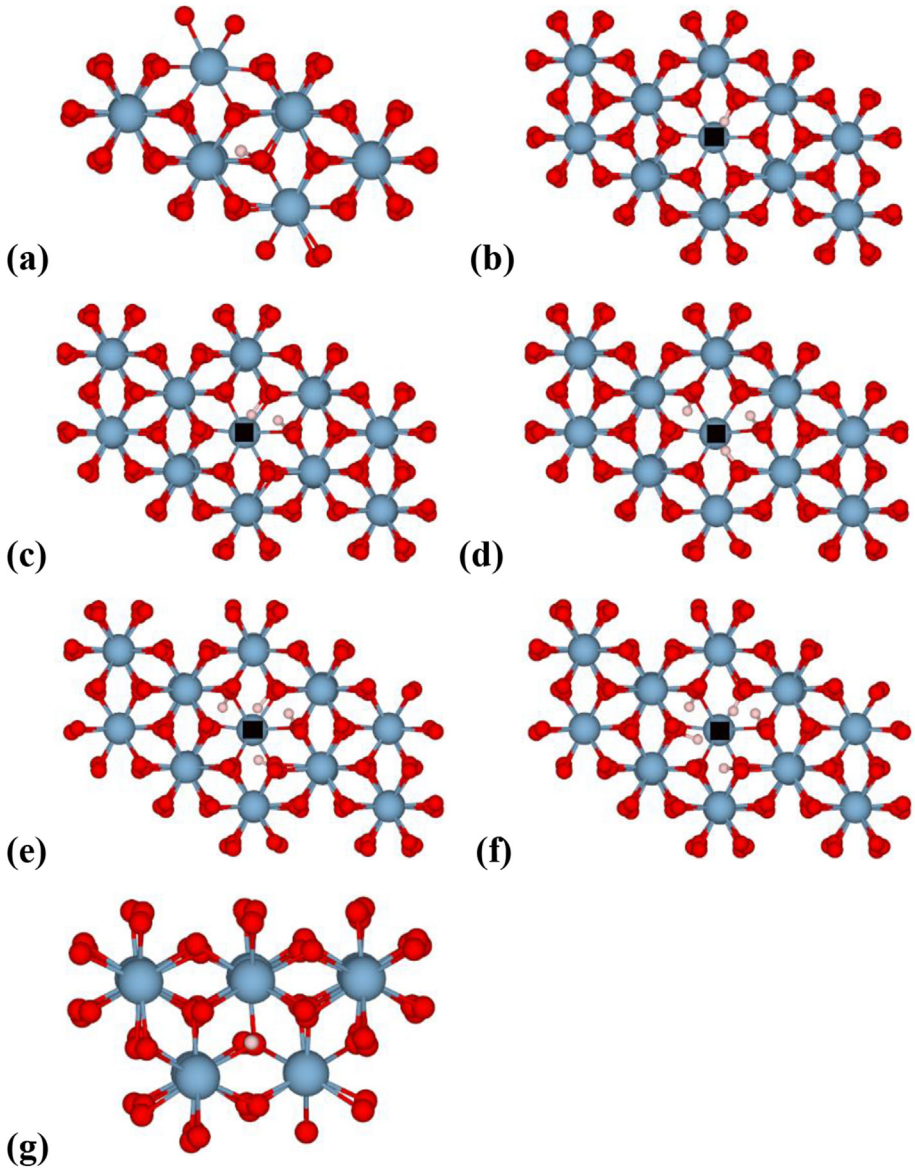

Fig. 3. Relaxed configurations of key hydrogen defects (a) $H_i^{\cdot}$ in the octahedral interstitial site (b) $[V_{Al} - H]^{''}$ (c) $[V_{Al} - 2H]^{'}$ (d) $[V_{Al} - 3H]^{x}$ (e) $[V_{Al} - 4H]^{\cdot}$ (f) $[V_{Al} - 5H]^{\cdot\cdot}$ (g) $H_O^{\cdot}$. Al atoms are in blue, oxygen atoms are in red, hydrogen is in white. The Al vacancy is marked in black. The direction of view is along [0001]. The figures were generated using the software VESTA [46]. (For interpretation of the references to color in this figure legend, the reader is referred to the Web version of this article.)

Table 1
Binding energy of various $[V_{Al} - nH]^{q}$ clusters.

Defect cluster	Binding energy (eV)
$[V_{Al} - H]^{''}$	3.24
$[V_{Al} - 2H]^{'}$	1.90
$[V_{Al} - 3H]^{x}$	1.99
$[V_{Al} - 4H]^{\cdot}$	0.912
$[V_{Al} - 5H]^{\cdot\cdot}$	0.248
$[V_{Al} - 6H]^{\cdot\cdot\cdot}$	−0.716

hand side term of Equation (5). The total H concentration is ~6.8×10^{-11} per f.u., the contribution to which comes almost entirely from bound defect complexes seen in Fig. 4a. This explains the superior hydrogen permeation resistance behavior of α-Al_2O_3; that is, most of the hydrogen is immobile, trapped at Al vacancy sites with high binding energy.

In Mg-doped α-Al_2O_3, as seen in Fig. 4b, the predominant defect is the neutral defect complex $[Mg_{Al} - H]^{x}$, and its concentration is nearly equal to that of Mg (1 ppm). The concentration of free $H_i^{\cdot}$ is nearly 10^7 times higher than the undoped case. This higher concentration of $H_i^{\cdot}$, along with the significant effect of binding energy (0.68 eV for $[Mg_{Al} - H]^{x}$), leads to the formation of the complex and a decrease in the concentration of isolated $Mg_{Al}^{'}$. The isolated $H_i^{\cdot}$ is compensated by the remaining isolated $Mg_{Al}^{'}$ (concentration ~2.3×10^{-9} per f.u.). The total concentration of hydrogen is almost dictated entirely by the dopant concentration due to the complex formation and thus is ~10^{-6} per f.u. This 10^4 times increase in the total concentration of hydrogen, as well as the 10^7 times increase in the concentration of diffusible hydrogen ($H_i^{\cdot}$) as compared to the undoped case, makes Mg an unfavorable dopant to be used for improving the barrier properties of α-Al_2O_3.

In contrast to the above two cases, in Si-doped α-Al_2O_3, hydrogen defects are not the predominant defects. Instead, the

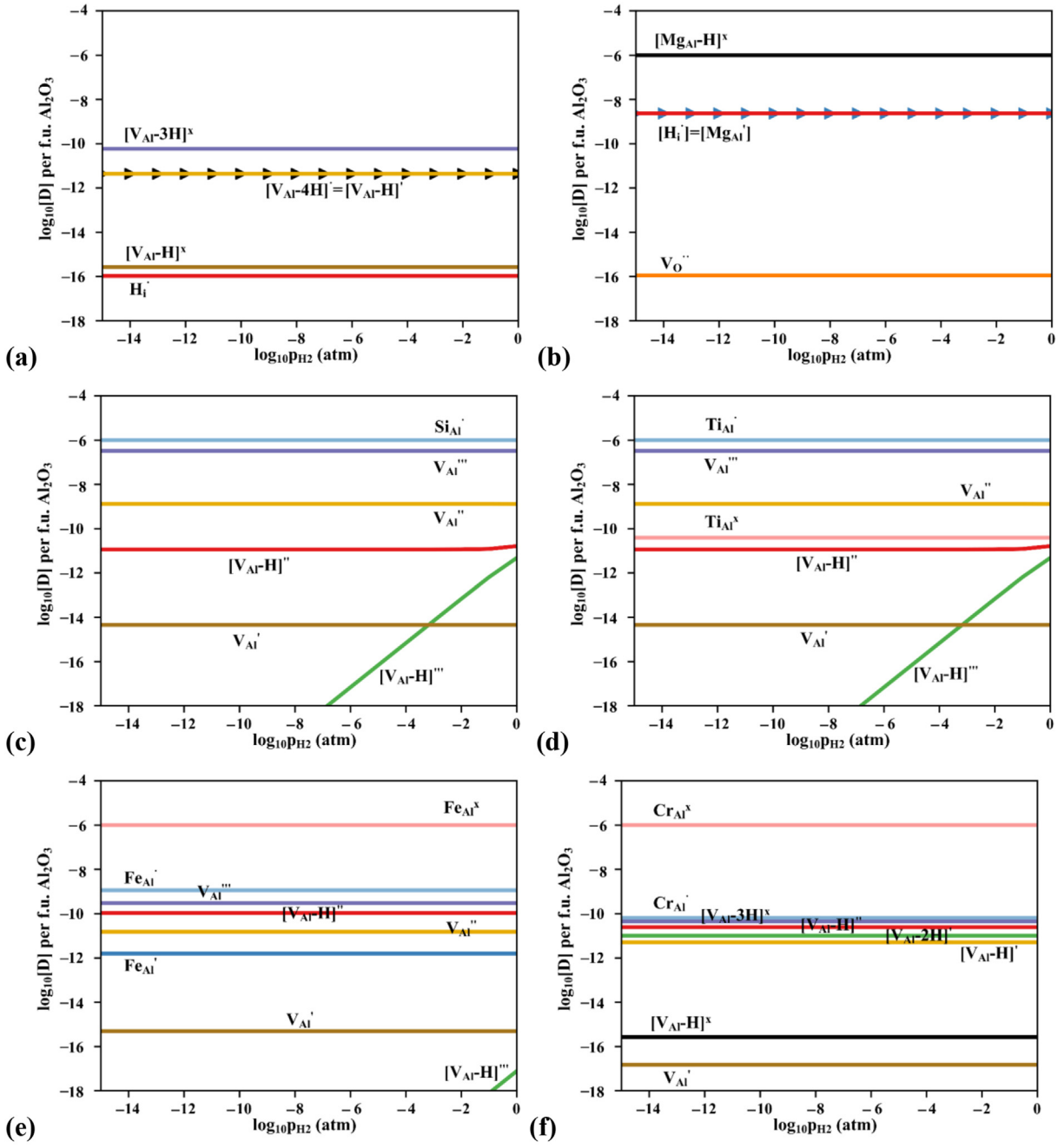

Fig. 4. Defect concentrations as a function of p_{H2} in (a) undoped (b) Mg-doped (c) Si-doped (d) Ti-doped (e) Fe-doped (f) Cr-doped α-Al_2O_3 at 300 K. Only those defects with concentration [D]>10^{-18} per f.u. α-Al_2O_3 are shown. Point defects are represented by Kröger-Vink notation.

predominant defects are $Si_{Al}^{\cdot}$ compensated by $V_{Al}^{\prime\prime\prime}$. The concentration of free hydrogen interstitial $H_i^{\cdot}$ is negligible (~10^{-59} per f.u.), due to its high formation energy at the equilibrium Fermi level established (see SI Fig. S7 for further discussion on equilibrium Fermi level effects on H_i^q concentration in the undoped and doped α-Al_2O_3 cases). This extremely low concentration of $H_i^{\cdot}$ offsets the effect of high binding energy and of the 10^3x increase in $V_{Al}^{\prime\prime\prime}$ concentration in the Si-doped system seen in Section 3.2 (which would have served to increase the concentration of $[V_{Al}-nH]^q$ as per Equation (5)). This ultimately reduces the concentration of hydrogen defect complexes as well. The $[Si_{Al}-H]^x$ complex concentration is also not significant, due to the low concentration of $H_i^{\prime}$.

The low concentrations of defect complexes in this case shows that not only does the binding energy of the defect complex matter, but the concentrations of the isolated individual defects also must be significant to ensure complex formation. It is worthwhile to point out here that this reduced concentration of free $H_i^{\cdot}$ and hydrogen defect complexes ultimately result in the overall hydrogen solubility to be lowered in Si-doped α-Al_2O_3 to nearly 1/3rd that of the undoped case. Additionally, it must be noted that diffusivity is also rapidly reduced, as hydrogen is present primarily in bound form in the lattice as $[V_{Al}-H]^{\prime\prime}$ and $[V_{Al}-H]^{\prime\prime\prime}$. These have high binding energies of 3.24 eV and 2.71 eV respectively. Thus, ultimately the overall permeability is likely to be lowered. Similar trend is seen in Ti-doped α-Al_2O_3. Thus, with Si- and Ti-doping of α-Al_2O_3, not only

does the total hydrogen concentration decrease to 1/3 that of the undoped case, the drastically lowered concentration of diffusible hydrogen $\left(H_i^q\right)$ and the presence of hydrogen predominantly in bound form will likely reduce the hydrogen diffusivity, resulting in an overall lowered permeability. This will improve the hydrogen permeation resistance properties of α-Al_2O_3.

The results are slightly different when the Fe-doped system is considered. The concentration of free hydrogen interstitial $H_i^{\cdot}$ at high p_{H2} is eliminated to negligible amounts (~10^{-55} per f.u.). This in turn decreases the concentration of $[V_{Al}-nH]^q$ and $[Fe_{Al}-H]^q$. However, the total hydrogen solubility, with the main contributors being $[V_{Al}-H]^{''}$ and $[V_{Al}-H]^{'''}$, is ~10^{-10} per f.u., around 1.5 times higher than that of the undoped system. This increase (though practically inconsequential), as compared to the 3 times decrease by Si and Ti dopants, can be attributed to the difference in the concentrations of $H_i^{\cdot}$: it is 10^{-55} per f.u. in the Fe-doped system, whereas it is 10^{-59} per f.u. in the Si and Ti-doped system. In the Fe-doped case, the concentration of hydrogen is unable to offset the effect of 10x increase in concentration of V_{Al}^q, leading to a slight increase in hydrogen solubility through the formation of defect complexes. Despite this slight increase in total hydrogen solubility, the diffusivity is likely to be reduced due the presence of hydrogen in primarily bound form as defect complexes with high binding energies. This will reduce the overall permeability of hydrogen in the system.

In Cr-doped α-Al_2O_3, unlike the previous Mg-, Si-, Ti- and Fe-doped cases, we see many types of hydrogen defect complexes with significant concentrations: $[V_{Al}-3H]^x$, $[V_{Al}-H]^{''}$, $[V_{Al}-2H]^{'}$, $[V_{Al}-H]^{'}$, $[V_{Al}-H]^x$. The concentration of free $H_i^{\cdot}$ is ~10^{-32} per f.u. (10^{-16} times that of the undoped case.) However, this isolated $H_i^{\cdot}$ concentration, although many orders of magnitude lower than the undoped case, is comparatively much higher than the other 4 doped cases considered above. This comparatively higher $H_i^{\cdot}$ concentration leads to the formation of defect complexes and clusters with $n>1$, unlike in Si, Ti, and Fe. The overall hydrogen solubility is slightly more than that of the undoped case by 1.25 times. This insignificant increase, and the presence of hydrogen in predominantly bound form with high binding energies and thus lowered diffusivity, will likely reduce the overall permeability in the system.

It must be clarified here that ultimately, it is the concentration of isolated vacancies $N_{V_{Al}^q}$, isolated hydrogen interstitials $(N_{H_i^q})^n$ and the binding energy E_b of the defect complex $[V_{Al}-nH]^q$ that together decide the effect of the dopant on the overall hydrogen solubility of the system. From practical considerations, the resulting defect concentration of free $H_i^{\cdot}$ as 10^{-59} per f.u. vs. 10^{-55} per f.u. vs. 10^{-32} per f.u. in the Si (and Ti)-, Fe- and Cr-doped cases respectively, though differing by orders of magnitude, are all uniformly negligible. It is only from a mathematical point of view (via Equation (5)) that slight differences in solubility arise. It can thus be said that doping with Si, Ti, Fe or Cr will all perform reasonably well to reduce the hydrogen permeability in α-Al_2O_3, due to the drastic reduction of mobile $H_i^{\cdot}$ concentration to negligible amounts and the presence of hydrogen in primarily bound defect complexes. This effect of isolated defect concentrations and binding energy on hydrogen diffusivity and solubility is elaborated upon in Section 3.5.

In none of the cases above do we see the electronic conductivity of α-Al_2O_3 increase upon H-addition. This is unlike what has been observed in other oxides like ZnO [48]. This is because in α-Al_2O_3, interstitial hydrogen is a deep donor, its defect level at 3.93 eV. In all the cases, the equilibrium Fermi level established is deep in the band gap (see SI Fig. S7), away from the conduction and valence band edges. The deep defect level is also seen in the density of states plot, shown in SI Fig. S8. Thus, interstitial hydrogen is compensated by other defects present in the oxide, without contributing to the electronic conductivity.

It must be emphasized here that the trends and predominant hydrogen defects revealed are also important while considering the effect of hydrogen in oxides used in other applications. One example as mentioned in Section 1 is that of resistive switching, in which the oxide electrolytes have exhibited sensitivity to humidity [24]. Knowledge of the defect state of hydrogen in the oxide by utilizing the methods employed in this study can help unambiguously establish the defect compensation mechanisms during device operation and elucidate the effect of hydrogen on device performance. Therefore, in Fig. 4, the x-axis can be replaced by voltage, which can be used in such devices to control the hydrogen concentration.

Fig. 5 summarizes the roles of the concentrations of $V_{Al}^{'''}$, $H_i^{\cdot}$ and $[V_{Al}-nH]^q$ ($[Mg_{Al}-H]^x$ for Mg-doped case) in determining the total concentration of H-defects, H_{tot}. Although other charge states of V_{Al} and H_i do contribute to the H-defect complexes and overall H concentration, we focus mainly on $V_{Al}^{'''}$ and $H_i^{\cdot}$ as they are involved in the maximum number of H-complexes and overall H concentration. The clear effect of donor dopants in eliminating $H_i^{\cdot}$ is seen in Fig. 5b. Fig. 5c shows that with Si and Ti doping, the low $H_i^{\cdot}$ offsets the increase in $V_{Al}^{'''}$ seen in Fig. 5a, leading to a decrease in the concentration of hydrogen-defect complexes relative to the undoped case. The trend in Fig. 5d matches exactly that in Fig. 5c, showing that in all cases, total hydrogen solubility is dictated by largely by H-defect complex concentration due to binding energy effects at low temperature. This figure summarizes the main results of our work.

3.5. Effect of varying dopant concentrations on hydrogen permeability

In the results presented above, the dopant concentration was fixed at 1 ppm. As mentioned in Section 2.2, this is simply a representative doping concentration, chosen to be within the solubility limit of the various dopants in α-Al_2O_3 and to ensure that the dilute defect approximation is still valid. However, a reasonable question arises, i.e., whether changing the dopant concentration will impact the relative trends in concentrations of free $H_i^{\cdot}$ (impacting hydrogen diffusivity) and the total concentration of hydrogen.

To answer this, two additional dopant concentrations were studied: 10 and 100 ppm. As seen in SI Fig. S9, at 1100 K, increase in dopant concentration leads to (i) increase in compensating defect concentrations and (ii) increase in transition p_{O2} for p-type to n-type conductivity in the Si and Ti donor doping cases. However, the relative trends in defect concentrations do not change with dopant concentration for the most part, except for the Cr-doped case. In the 1 ppm Cr-doped case, holes are the 2nd predominant defect, whereas in the 10 and 100 ppm Cr-doped cases, $Cr_{Al}^{\cdot}$ is the 2nd predominant defect.

Fig. 6 shows the effect of doping levels on the concentrations of $V_{Al}^{'''}$, $H_i^{\cdot}$ and $[V_{Al}-nH]^q$ ($[Mg_{Al}-H]^x$ for Mg-doped case), which ultimately determine hydrogen diffusivity and solubility (similar to Fig. 5). From Fig. 6a it is clear that increase in Si and Ti concentration by 10x and 100x leads to a corresponding increase in $V_{Al}^{'''}$ concentration, due to the exact compensation of $Si_{Al}^{\cdot}$ and $Ti_{Al}^{\cdot}$ by $V_{Al}^{'''}$. Increase in $V_{Al}^{'''}$ in the Fe and Cr doped cases is not as high, as Fe and Cr are predominantly isovalent in α-Al_2O_3. Fig. 6b shows that despite an increase in Mg, Si, and Ti concentration, the free $H_i^{\cdot}$

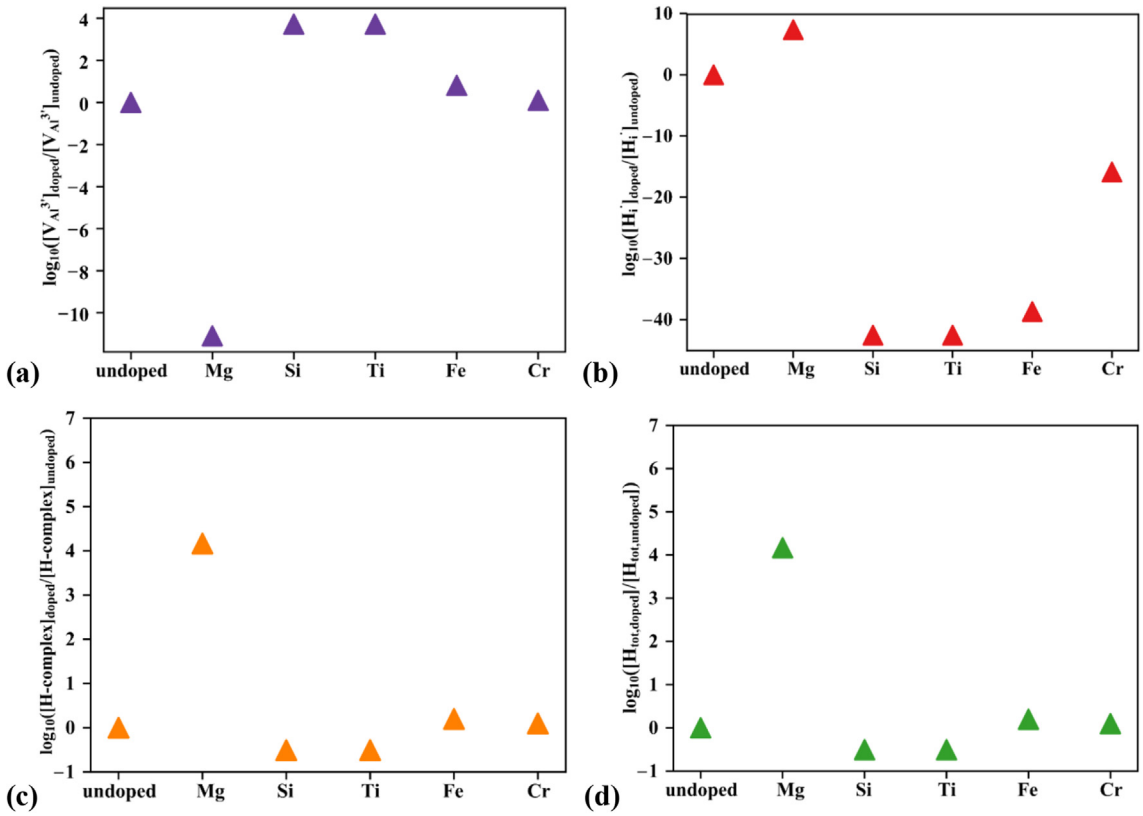

Fig. 5. Normalized (a) $V_{Al}^{'''}$ concentrations obtained at 1100 K, $p_{O2} = 1$ atm (b) $H_i^{\cdot}$ concentrations (c) H-complex concentrations (d) H_{tot} concentrations, all obtained at 300 K, $p_{H2} = 1$ atm, as a function of dopant.

concentration does not change significantly for these dopants. This is because the Fermi level in these cases is effectively pinned by the charged ionic defect with the largest (fixed) concentration (therefore the pinning effect is strongest for Mg, Si and Ti), and changing dopant concentration by 10x or 100x is not enough to change the Fermi level significantly. The pinning effect isn't as strong for Fe and is the least strong for Cr as these are primarily isovalent in α-Al_2O_3. Although a large drop in $H_i^{\cdot}$ concentration is seen in the Cr doped case as the concentration is changed from 1 to 10 ppm, this drop is still negligible at the scale considered (the absolute $H_i^{\cdot}$ defect concentrations in donor doped cases are of the order 10^{-55} ppm). Thus, increase in dopant concentration does not have a significant effect on concentration of diffusible $H_i^{\cdot}$. From Fig. 6c we see that an increase in Mg concentration to 10 and 100 ppm leads to an increase in $[Mg_{Al} - H]^x$ concentration, as expected. However, increasing Si and Ti doping to 10 and 100 ppm leads to an increase in hydrogen complex concentration by 2x and 12x respectively, compared to the undoped case. This increase (as opposed to the decrease in hydrogen complex concentration when Si and Ti doping was 1 ppm) is due to the increase in $V_{Al}^{'''}$ concentration, which increases the complex concentration via Equation (5). The decrease in $H_i^{\cdot}$ upon increased Si and Ti doping is not enough to offset the effect of increased $V_{Al}^{'''}$ concentration. At 10 ppm Fe, the H-complex concentration remains nearly the same as that in the undoped case. However, at 100 ppm, Fe reduces the hydrogen complex solubility by 2x, compared to the undoped case. This is because at this concentration, the decrease in $H_i^{\cdot}$ concentration is enough to offset the slight increase in $V_{Al}^{'''}$, leading to a net decrease in overall concentration of H-complexes. Cr doping at 10 ppm slightly increases the H-complex concentration by 2x, and at 100 ppm the H-complex concentration remains nearly equal to that in the undoped case. Finally, the total hydrogen concentration follows the trend of the hydrogen complex concentrations, due to the significant binding energy effects at low temperature. Thus, an increase in the Si and Ti concentrations *increases* the total hydrogen concentration by ~2x (10 ppm doping) and ~12x (100 ppm doping). At 100 ppm, only Fe reduces the overall solubility by 2x.

This effect of varying dopant concentrations brings us back to the point mentioned in Section 3.4 that it is the concentration of isolated vacancies $N_{V_{Al}^q}$, isolated hydrogen interstitials $(N_{H_i^q})^n$ and the binding energy E_b of the defect complex $[V_{Al} - nH]^q$ that together decide the effect of the dopant on the overall hydrogen solubility of the system. Increasing the dopant concentration does not change the free $H_i^{\cdot}$ concentration (and in turn, the hydrogen diffusivity) significantly. Thus, donor dopants like Si, Ti, Fe and Cr, with their near negligible $H_i^{\cdot}$ concentrations and hydrogen predominantly present in complex form, will aid in reducing hydrogen permeability. Moreover, doping Si and Ti at 1 ppm gave the best results, as in addition to lowered diffusivity due to near negligible concentration of $H_i^{\cdot}$, the total hydrogen concentration is reduced by 3x at this lower doping level, compared to the 2x decrease exhibited by doping Fe at 100 ppm. Thus, doping α-Al_2O_3 with Si and Ti at 1 ppm appears to be the overall best strategy to reduce its hydrogen permeability.

4. Conclusions

To create better hydrogen permeation barriers, experimental and theoretical work related to the behavior of hydrogen in α-Al_2O_3, a popular coating material, and ways to improve its adherence onto

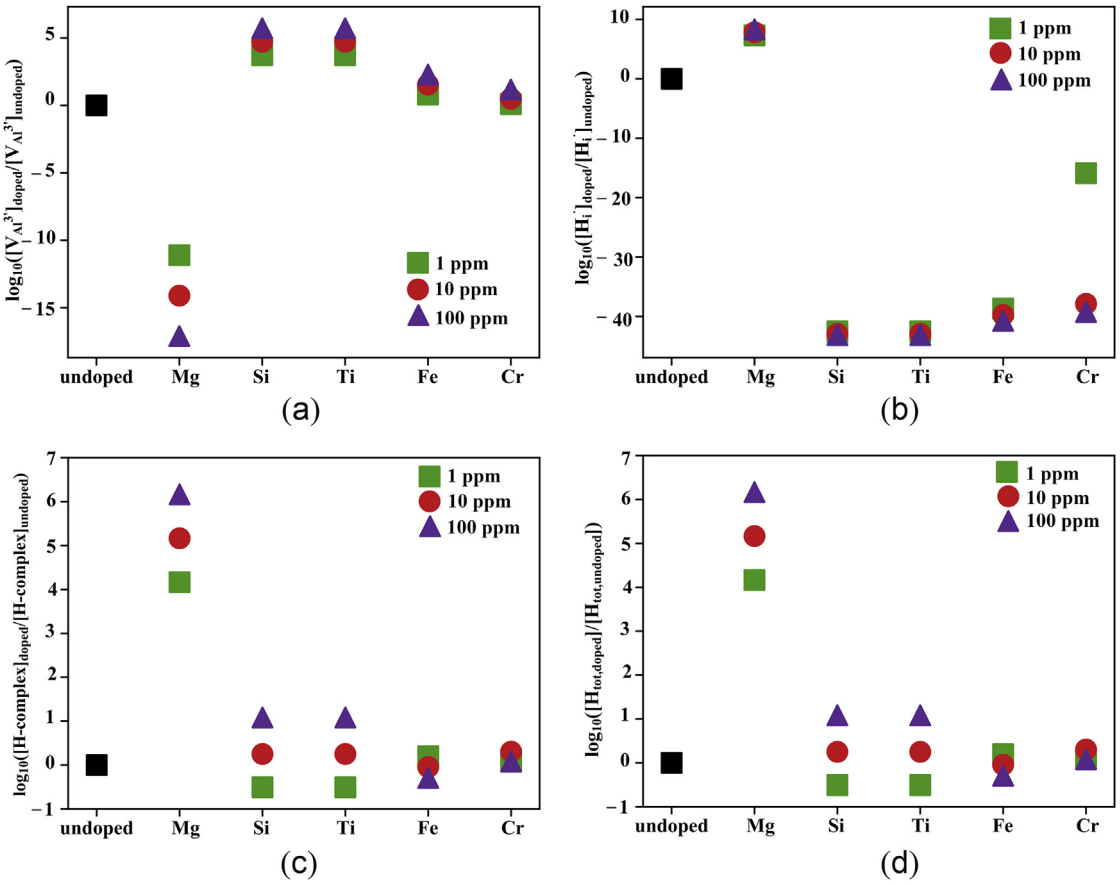

Fig. 6. Normalized (a) $V_{Al}^{'''}$ concentrations obtained at 1100 K, $p_{O2} = 1$ atm (b) $H_i^{\bullet}$ concentrations (c) H-complex concentrations (d) H_{tot} concentrations, all obtained at 300 K, $p_{H2} = 1$ atm, as a function of dopant, with dopant concentration = 1, 10, 100 ppm.

steel, already exist. This study systematically assessed the effect of dopants to further reduce hydrogen permeation in α-Al_2O_3. Our analysis took into account the equilibrium high temperature defect concentrations during α-Al_2O_3 formation, and the binding energy effects at low temperature to find the defect concentrations during hydrogen-rich operating conditions. In the undoped case, the predominant hydrogen defect is $[V_{Al} - 3H]^x$, a defect complex with high binding energy. This gives insights into the reason behind the superior performance of α-Al_2O_3 as a hydrogen permeation barrier: hydrogen predominantly exists as clusters trapped on the $V_{Al}^{'''}$ site, which presumably increases the activation energy for migration in the lattice. Analyzing the effect of dopants, with the doping level fixed at 1 ppm, it was found that the impact on the total hydrogen concentration H_{tot} (with consequences on solubility) and the concentration of free hydrogen interstitials $H_i^{\bullet}$ (with consequences on diffusivity) is distinct and substantial. In Mg-doped α-Al_2O_3, both H_{tot} and isolated $H_i^{\bullet}$ concentrations are higher than in the undoped case by 10^4 and 10^7 times respectively. This makes Mg an unsuitable choice for a dopant for improving the properties of α-Al_2O_3 as a hydrogen permeation barrier. In both Fe- and Cr-doped α-Al_2O_3, H_{tot} increases slightly by 1.5 times and 1.25 times respectively, however, the more mobile species $H_i^{\bullet}$ is found to be literally eliminated. Thus, although Fe and Cr doping increase the hydrogen solubility slightly, the hydrogen is trapped on the V_{Al}^{q} sites with high binding energies in the form of $[V_{Al} - nH]^q$. This implies that doping with Fe and Cr could help reduce the overall permeability by reducing the diffusivity of hydrogen in the lattice. The best dopants were found to be Si and Ti. These reduce H_{tot} to nearly 1/3 that of the undoped case. Additionally, the more mobile species $H_i^{\bullet}$ is eliminated. Thus, upon Si and Ti doping, the overall permeability will be reduced because the solubility is lower and most of the hydrogen present is trapped on the V_{Al}^{q} sites with high binding energy (~3 eV) in the form of $[V_{Al} - H]^{''}$ and $[V_{Al} - H]^{'''}$, thus reducing diffusivity. Comparing these results obtained at 1 ppm doping level with those obtained at doping levels of 10 and 100 ppm, doping α-Al_2O_3 with Si and Ti at 1 ppm was found to be the overall best strategy that reduced both hydrogen diffusivity and solubility by the greatest amount. The established effects of the dopants on electrical properties of α-Al_2O_3 and on the predominant hydrogen defects in the lattice can also be extended to other applications such as resistive switching, where electrical conductivity, hydrogen defects, and defect compensation mechanisms play a significant role in determining device performance.

Acknowledgements

This work was supported by Exelon Corporation, a Fortune 100 company that works in power generation, energy sales, transmission and delivery and is one of Unites States' largest competitive power generators. We acknowledge the Extreme Science and Engineering Discovery Environment (XSEDE) Stampede2 resource at the Texas Advanced Computing Center for calculations performed under allocation number TG-DMR120025. We thank Dr. Lixin Sun, Jing Yang and Dr. Franziska Hess for helpful discussions regarding the DFT simulations and thermodynamic modeling. We are also grateful to Dr. Xiahui Yao and Dr. William Bowman for critical reading of the manuscript.

Appendix A. Supplementary data

Supplementary data to this article can be found online at https://doi.org/10.1016/j.actamat.2019.02.031.

References

[1] J. Yamabe, T. Awane, S. Matsuoka, Elucidating the hydrogen-entry-obstruction mechanism of a newly developed aluminum-based coating in high-pressure gaseous hydrogen, Int. J. Hydrog. Energy 40 (32) (2015) 10329–10339.

[2] B. Zajec, Hydrogen permeation barrier–recognition of defective barrier film from transient permeation rate, Int. J. Hydrog. Energy 36 (12) (2011) 7353–7361.

[3] G. Zhang, S. Dou, Y. Lu, Y. Shi, X. Lai, X. Wang, Mechanisms for adsorption, dissociation and diffusion of hydrogen in hydrogen permeation barrier of α-Al_2O_3: the role of crystal orientation, Int. J. Hydrog. Energy 39 (1) (2014) 610–619.

[4] G. Zhang, Y. Lu, X. Wang, Hydrogen interactions with intrinsic point defects in hydrogen permeation barrier of α-Al_2O_3: a first-principles study, Phys. Chem. Chem. Phys. 16 (33) (2014) 17523–17530.

[5] G. Zhang, X. Wang, Y. Xiong, Y. Shi, J. Song, D. Luo, Mechanism for adsorption, dissociation and diffusion of hydrogen in hydrogen permeation barrier of α-Al_2O_3: a density functional theory study, Int. J. Hydrog. Energy 38 (2) (2013) 1157–1165.

[6] G. Hollenberg, E. Simonen, G. Kalinin, A. Terlain, Tritium/hydrogen barrier development, Fusion Eng. Des. 28 (1995) 190–208.

[7] R.H. Jones, G.J. Thomas, Materials for the Hydrogen Economy, CRC Press, 2007.

[8] H.K.D.H. Bhadeshia, Prevention of hydrogen embrittlement in steels, ISIJ Int. 56 (1) (2016) 24–36.

[9] R.M. Roberts, T.S. Elleman, H.P III, K. Verghese, Hydrogen permeability of sintered aluminum oxide, J. Am. Ceram. Soc. 62 (9-10) (1979) 495–499.

[10] R.A. Oriani, The diffusion and trapping of hydrogen in steel, Acta Metall. 18 (1) (1970) 147–157.

[11] J. Fowler, D. Chandra, T. Elleman, A. Payne, K. Verghese, Tritium diffusion in Al_2O_3 and BeO, J. Am. Ceram. Soc. 60 (3-4) (1977) 155–161.

[12] K. Forcey, D. Ross, J. Simpson, D. Evans, A. Whitaker, The use of aluminising on 317 austenitic and 1.4914 martensitic steels for the reduction of tritium leakage from the net blanket, J. Nucl. Mater. 161 (2) (1989) 108–116.

[13] K. Forcey, D. Ross, C. Wu, The formation of hydrogen permeation barriers on steels by aluminising, J. Nucl. Mater. 182 (1991) 36–51.

[14] A.B. Belonoshko, A. Rosengren, Q. Dong, G. Hultquist, C. Leygraf, First-principles study of hydrogen diffusion in α–Al_2O_3 and liquid alumina, Phys. Rev. B 69 (2) (2004) 024302.

[15] H. Engstrom, J.B. Bates, J. Wang, M. Abraham, Infrared spectra of hydrogen isotopes in α-Al_2O_3, Phys. Rev. B 21 (4) (1980) 1520.

[16] A. Kronenberg, J. Castaing, T. Mitchell, S. Kirby, Hydrogen defects in α-Al_2O_3 and water weakening of sapphire and alumina ceramics between 600 and 1000° C—I. Infrared characterization of defects, Acta Mater. 48 (7) (2000) 1481–1494.

[17] A. Aiello, A. Ciampichetti, G. Benamati, An overview on tritium permeation barrier development for WCLL blanket concept, J. Nucl. Mater. 329 (2004) 1398–1402.

[18] J. Konys, W. Krauss, N. Holstein, Development of advanced Al coating processes for future application as anti-corrosion and T-permeation barriers, Fusion Eng. Des. 85 (10–12) (2010) 2141–2145.

[19] H. Yang, Q. Zhan, W. Zhao, X. Yuan, Y. Hu, Z. Han, Study of an iron-aluminide and alumina tritium barrier coating, J. Nucl. Mater. 417 (1–3) (2011) 1237–1240.

[20] F. Kröger, Defect related properties of doped alumina, Solid State Ionics 12 (1984) 189–199.

[21] M. Youssef, M. Yang, B. Yildiz, Doping in the valley of hydrogen solubility: a route to designing hydrogen-resistant zirconium alloys, Physical Review Applied 5 (1) (2016) 014008.

[22] Z. Wang, W. Zhu, A. Du, L. Wu, Z. Fang, X.A. Tran, W. Liu, K. Zhang, H.-Y. Yu, Highly uniform, self-compliance, and forming-free ALD HfO_2-based RRAM with Ge doping, IEEE Trans. Electron Devices 59 (4) (2012) 1203–1208.

[23] D. Lee, D.-j. Seong, H. jung Choi, I. Jo, R. Dong, W. Xiang, S. Oh, M. Pyun, S.-o. Seo, S. Heo, Excellent Uniformity and Reproducible Resistance Switching Characteristics of Doped Binary Metal Oxides for Non-volatile Resistance Memory Applications, Electron Devices Meeting, 2006. IEDM'06, International, IEEE, 2006, pp. 1–4.

[24] S. Tappertzhofen, I. Valov, T. Tsuruoka, T. Hasegawa, R. Waser, M. Aono, Generic relevance of counter charges for cation-based nanoscale resistive switching memories, ACS Nano 7 (7) (2013) 6396–6402.

[25] H. Yoon, M. Choi, T.-W. Lim, H. Kwon, K. Ihm, J.K. Kim, S.-Y. Choi, J. Son, Reversible phase modulation and hydrogen storage in multivalent VO_2 epitaxial thin films, Nat. Mater. 15 (10) (2016) 1113.

[26] L.Q. Zhu, C.J. Wan, L.Q. Guo, Y. Shi, Q. Wan, Artificial synapse network on inorganic proton conductor for neuromorphic systems, Nat. Commun. 5 (2014) 3158.

[27] G. Kresse, D. Joubert, From ultrasoft pseudopotentials to the projector augmented-wave method, Phys. Rev. B 59 (3) (1999) 1758.

[28] J.P. Perdew, K. Burke, M. Ernzerhof, Generalized gradient approximation made simple, Phys. Rev. Lett. 77 (18) (1996) 3865.

[29] G. Kresse, J. Furthmüller, Efficiency of ab-initio total energy calculations for metals and semiconductors using a plane-wave basis set, Comput. Mater. Sci. 6 (1) (1996) 15–50.

[30] G. Makov, M. Payne, Periodic boundary conditions in ab initio calculations, Phys. Rev. B 51 (7) (1995) 4014.

[31] J. Robertson, High dielectric constant oxides, Eur. Phys. J. Appl. Phys. 28 (3) (2004) 265–291.

[32] S. Kasamatsu, T. Tada, S. Watanabe, Theoretical analysis of space charge layer formation at metal/ionic conductor interfaces, Solid State Ionics 183 (1) (2011) 20–25.

[33] L. Wang, T. Maxisch, G. Ceder, Oxidation energies of transition metal oxides within the GGA+ U framework, Phys. Rev. B 73 (19) (2006) 195107.

[34] M. Chase, C. Davies, J. Downey, D. Frurip, R. Mcdonald, A. Syverud , NIST-JANAF thermodynamic tables, J. Phys. Chem. Ref. Data Monograph 9 (1998).

[35] A. Heuer, Oxygen and aluminum diffusion in α-Al_2O_3: how much do we really understand? J. Eur. Ceram. Soc. 28 (7) (2008) 1495–1507.

[36] J. Heyd, G.E. Scuseria, M. Ernzerhof, Hybrid functionals based on a screened Coulomb potential, J. Chem. Phys. 118 (18) (2003) 8207–8215.

[37] M. Choi, A. Janotti, C.G. Van de Walle, Native point defects and dangling bonds in α-Al_2O_3, J. Appl. Phys. 113 (4) (2013) 044501.

[38] K. Kitazawa, R. Coble, Electrical conduction in single-crystal and polycrystalline Al_2O_3 at high temperatures, J. Am. Ceram. Soc. 57 (6) (1974) 245–250.

[39] P.W. Levy, Annealing of the defects and colour centres in unirradiated and in reactor irradiated Al_2O_3, Discuss. Faraday Soc. 31 (1961) 118–129.

[40] S. Mohapatra, F. Kröger, Defect structure of alpha-Al_2O_3 doped with magnesium, American Ceramic Society, Journal 60 (1977) 141–148.

[41] J. Rasmussen, W. Kingery, Effect of dopants on the defect structure of single-crystal aluminum oxide, J. Am. Ceram. Soc. 53 (8) (1970) 436–440.

[42] S. Mohapatra, F. Kröger, Defect structure of α-Al_2O_3 doped with titanium, J. Am. Ceram. Soc. 60 (9-10) (1977) 381–387.

[43] B. Dutt, F. Kröger, High-temperature defect structure of iron-doped α-alumina, J. Am. Ceram. Soc. 58 (11-12) (1975) 474–476.

[44] G.W. Hollenberg, R.S. Gordon, Effect of oxygen partial pressure on the creep of polycrystalline Al_2O_3 doped with Cr, Fe, or Ti, J. Am. Ceram. Soc. 56 (3) (1973) 140–147.

[45] S.N. Rashkeev, K.W. Sohlberg, S. Zhuo, S.T. Pantelides, Hydrogen-induced initiation of corrosion in aluminum, J. Phys. Chem. C 111 (19) (2007) 7175–7178.

[46] K. Momma, F. Izumi, VESTA 3 for three-dimensional visualization of crystal, volumetric and morphology data, J. Appl. Crystallogr. 44 (6) (2011) 1272–1276.

[47] T. Turner, J. Crawford Jr., V centers in single crystal Al_2O_3, Solid State Commun. 17 (2) (1975) 167–169.

[48] C.G. Van de Walle, Hydrogen as a cause of doping in zinc oxide, Phys. Rev. Lett. 85 (5) (2000) 1012.